

Increased robustness for fluidic self-assembly

Mekala Krishnan,¹ Michael T. Tolley,¹ Hod Lipson,^{1,2} and David Erickson^{1,a)}

¹*Sibley School of Mechanical and Aerospace Engineering, Cornell University, Ithaca, New York 14853, USA*

²*Computing and Information Science, Cornell University, Ithaca, New York 14853, USA*

(Received 15 December 2007; accepted 12 June 2008; published online 21 July 2008)

Self-assembly methods have been developed at the micro- and nanoscale to create functional structures from subelements stochastically dispersed in a fluid. Self-assembly paradigms have limitations in terms of achievable complexity of the final structure, ability to perform error correction, and scalability. Fluidic self-assembly attempts to overcome these limitations by incorporating a controlled flow structure and/or complex geometric interactions to improve the assembly rate and the specificity of the final positioning. Since the initial position and orientation of a subelement in a stochastic system are indeterminate, the most robust of these schemes are those for which the dependence on the initial condition will be the weakest. In this paper we develop an analytical/numerical model for the fluid forces and torques on a two-dimensional subelement involved in a fluidic self-assembly process and describe the translational and rotational motions of the element due to these forces. We use this model to determine optimal subelement shapes and flow conditions that lead to successful assembly over the broadest range of initial conditions. We quantify the degree to which assembly has been successful by introducing two docking parameters that are descriptive of how close the final subelement position is to the ideal case. Robust self-assembly schemes were developed for the assembly of different tile shapes. This approach to evaluate a self-assembly process based on the final subelement position can be applied to other fluidic self-assembly techniques. © 2008 American Institute of Physics. [DOI: 10.1063/1.2957712]

I. INTRODUCTION

As an alternative to traditional “top-down” fabrication techniques,¹ self-assembly^{2,3} is a “bottom-up” method whereby a target structure is constructed from a set of small scale subelements with as little external intervention as possible. The subelements represent the fundamental building blocks of the final device and can be manufactured or synthesized at any time prior to the final assembly. Top-down device fabrication approaches based on lithography are essentially two dimensional (2D) in nature and require that the various components of a device be manufactured using compatible fabrication technologies. Self-assembly offers distinct advantages over these top-down fabrication techniques in that they enable the fabrication of three dimensional (3D) structures⁴ from nonuniform subelements. This could potentially enable designers to build devices comprising complex arrays of different materials or functionalities which would be impossible to achieve using traditional microfabrication techniques.⁵ These self-assembly techniques also offer potential advantages at the microscale over traditional pick and place methods including spatial resolution (since very small subelements can be synthesized), higher assembly rates (due to increased parallelism), lower device costs (since the amount of infrastructure required can be lower), and fewer problems with undesired adhesion.⁶

Various self-assembly paradigms exist that make use of interelement affinities in scales ranging from the mesoscopic to the macroscopic.⁷ These affinities include noncovalent at-

tractions such as van der Waals, hydrophobic, and Coulomb interactions, as well as covalent interactions.^{3,8,9} More recently, fluid based interactions have been studied as the driving mechanism for self-assembly that can be classified under fluidic self-assembly. Capillary interactions that are based on the minimization of free energies at interfacial areas have been used to carry out assembly of components at fluid interfaces as well as in suspension.^{10,11} These interactions have been used to fabricate devices with micromirrors¹² and light emitting diodes.^{13,14} Fluidic self-assembly has also been applied to the assembly of patterned subelements on a substrate using shape matching, where a suspension of components is made to flow across a substrate having indentations complementary to the shape of the components, causing the components to fall into and subsequently bind to the indentations.^{15,16} Finally, fluid forces have been coupled with other forces such as colloidal interactions,¹⁷ magnetic forces,^{18,19} and optical forces²⁰ to extend fluidic self-assembly to a broader range of assembly applications.

The self-assembly methods described above are largely stochastic in nature and rely on large component numbers to carry out successful assembly and reduce errors. This approach has certain drawbacks. These techniques lend themselves well to the building of regular structures rather than irregular shapes which reduces the scope of applications for these methods. Additionally, as the complexity of the target structure increases, more distinct types of pieces are needed to carry out assembly, lowering the selectivity of intercomponent affinities and increasing the probability of error. Finally, since the affinity between two components is often

^{a)}Electronic mail: de54@cornell.edu.

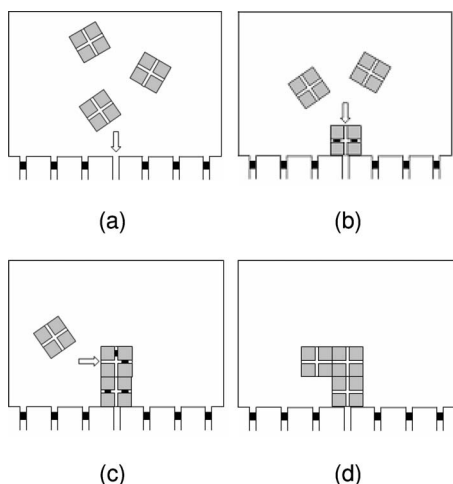


FIG. 1. Schematic depicting DHFSA. (a) shows the attraction of a tile, moving stochastically in the fluid, to the substrate; (b) and (c) depict the building of the target structure by controlling the attraction basin through on-board valving; (d) shows the final assembled structure.

shape dependent, the shape of the assembling components must be carefully designed for each new target structure, which makes these self-assembly procedures less robust and scalable.

We have recently developed a semidirected deterministic assembly process, directed hierarchical fluidic self-assembly (DHFSA), which attempts to address these shortcomings.^{21,22} In this method, the assembly of subelements takes place in a microfluidic chamber with directed fluid motion being the driving mechanism for the assembly. The chamber is lined with an array of ports along its sides through which fluid can flow into and out of the chamber. The motion of fluid exerts both force and torque on an assembling component, resulting in a translational and an angular velocity that move it to the target location. Figure 1 is a schematic showing of our concept of DHFSA. The assembling components shown here are 2D subelements (which we refer to as tiles herein), though assembly can be extended to three dimensions. The process begins with fluid flow into one of the substrate ports attracting a tile moving stochastically in the fluid toward it [Fig. 1(a)]. Once the tile attaches to the substrate, it can draw power from the substrate to activate on-board valves and direct fluid flow through internal channels in the tile [Fig. 1(b)]. This sink flow creates a local “attraction basin” along one of the tile faces, thus controlling the physical location where the next tile attaches [Fig. 1(b)]. The tiles join together through a reversible mechanical interaction. This process is continued to yield the desired target structure [Figs. 1(c) and 1(d)]. Validating the feasibility of the above concept, we have demonstrated the assembly and manipulation of passive tiles using DHFSA and have also carried out fabrication work to implement mechanical latches and electronic functionality on silicon tiles,²² as well as a valving mechanism based on on-board microvalves.²¹ On-board electronic functionality allows a tile to draw power from the substrate to activate the microvalves on the tile, thus paving the way for the DHFSA system described above. Using DHFSA, it is possible to implement error correction measures to reject in-

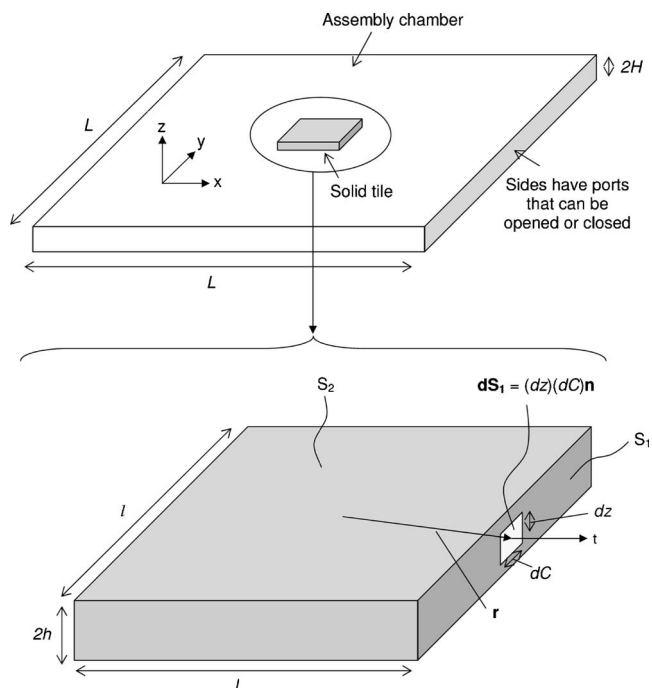


FIG. 2. Schematic of assembly chamber with magnified view of tile showing area vectors.

correctly assembled components and replace them with new parts, which is difficult to do using traditional self-assembly techniques. Since the tiles are themselves lithographically patterned, it is possible to implement microelectromechanical system functionality, chemistry, and microfluidics on the assembling components. These robust, scalable properties allow us to apply DHFSA to the assembly of novel laboratory-on-a-chip devices, new materials, and autonomously reconfigurable microsystems.

In self-assembly methods (including DHFSA) the initial position and orientation of a subelement involved in an assembly event are stochastic and therefore indeterminate. This complicates the overall process since the localized flow structure which guides the final assembly process (referred to herein as “docking”) will be successful only over a narrow range of initial conditions. Subelements which enter the attraction basin surrounding the docking position outside of this range will either not assemble or assemble incorrectly, resulting in a structural error. As such the most robust and rapid assembly scheme is one in which a successful assembly event can be assured for the widest range of initial conditions.

In this paper we describe the development of an analytical model describing the motion of a solid tile in a high aspect ratio microchamber (Fig. 2). Using numerical simulations this tile is subject to a range of different flow conditions and docking geometries with the goal of determining the conditions which maximize the range of initial positions and orientations that result in successful assembly. Previous work on modeling the driving force in a self-assembly process has been carried out for processes driven by magnetic forces,^{23–25} evaporation induced self-assembly,²⁶ and surface tension or capillary effects.^{27–29} However, the effect of modulating fluid

motion as an active mechanism for self-assembly has not to our knowledge been previously studied. Authors^{27–29} have studied the modeling of capillary effects and the design of suitable binding sites for their assembly procedure based on this model. Their approach to the characterization of successful docking and corresponding binding site design is based on free energy minimization (i.e., a good binding site design in one where the free energy of the system on docking has a unique minimum over the broadest range of initial tile orientations and positions). This approach works well for equilibrium driven self-assembly processes but is difficult to apply to dynamic (i.e., nonequilibrium) processes such as DHFSA. Instead, in order to quantitatively evaluate a successful assembly event in DHFSA, we describe two docking parameters that are based on the final position and orientation of the tile rather than on the free energy of the system. This approach allows us to design successful assembly schemes for DHFSA and could also be extended to other nonequilibrium methods of fluidic self-assembly. Our fluidic system is a multiphase system, where the solid tiles in the chamber interact with the liquid phase or the fluid in the chamber. Previous work on modeling the interaction between moving solid and liquid phases has been carried out, though mainly for shapes such as solid spheres,^{30–35} cylinders,^{36,37} or disks³⁸ in a fluidic medium where various approximations based on the shape can be applied and for fairly simple flow fields.

In Sec. II we begin by describing our analytical model and our method for capturing all the relevant 3D fluid mechanics with a 2D solution. This approach significantly reduces computational time, increases mesh element quality, and is therefore more amenable to future extension to a multiparticle system. In Sec. III the model is validated both through comparison with experimental results and full 3D simulations. In Sec. III the model is applied to a series of different tile shapes, chamber geometries, and flow conditions to determine the optimal set for assembly. We also introduce a set of “docking parameters” which serve to quantify successful assembly.

II. MATHEMATICAL MODEL

A solid body in a fluid medium experiences a translational force and a rotational torque as a result of the shear and pressure forces incident on it. Consider a solid tile in a chamber as shown in Fig. 2. The x and y dimensions of the body are l , while the z dimension thickness of the body is $2h$, where $2h \ll l$. The x and y dimensions of the chamber are $\sim L$ while the z dimension is $2H$, where again $2H \ll L$. The chamber has fluid inlet ports along its sides which can be opened to allow fluid to enter or leave the chamber or closed off to prevent fluid flow through them.

The fluid velocity \mathbf{v} within the chamber is governed by the continuity and Navier–Stokes equations, which for a constant property Newtonian fluid of density ρ and viscosity μ are given by Eqs. (1) and (2), respectively,

$$\nabla \cdot \mathbf{v} = 0, \quad (1)$$

$$\rho \left(\frac{\partial \mathbf{v}}{\partial t} + \mathbf{v} \cdot \nabla \mathbf{v} \right) = -\nabla p + \mu \nabla^2 \mathbf{v}. \quad (2)$$

The linear, \mathbf{a} , and angular, $\boldsymbol{\alpha}$, accelerations of the body within this flow field are calculated using the total stress tensor as

$$\mathbf{a} = \frac{\mathbf{F}}{m_{\text{tile}}} = \frac{\mathbf{F}_p + \mathbf{F}_v}{m_{\text{tile}}} = \frac{1}{m_{\text{tile}}} \left(- \oint_S p \mathbf{I} \cdot d\mathbf{S} + \oint_S \boldsymbol{\tau} \cdot d\mathbf{S} \right), \quad (3a)$$

$$\begin{aligned} \boldsymbol{\alpha} &= \frac{\mathbf{T}}{I_{\text{tile}}} = \frac{\mathbf{T}_p + \mathbf{T}_v}{I_{\text{tile}}} \\ &= \frac{1}{I_{\text{tile}}} \left(- \oint_S \mathbf{r} \times p \mathbf{I} \cdot d\mathbf{S} + \oint_S \mathbf{r} \times \boldsymbol{\tau} \cdot d\mathbf{S} \right), \end{aligned} \quad (3b)$$

where \mathbf{F} and \mathbf{T} are the force and torque on the tile, respectively, the subscript p refers to pressure force or torque, the subscript v refers to viscous force or torque, p is the pressure, $\boldsymbol{\tau}$ is the viscous stress tensor, \mathbf{I} is the identity tensor, \mathbf{S} is the total surface area of the tile, \mathbf{r} is a vector from the center of the tile to the boundary, m_{tile} is the mass of the tile, and I_{tile} is the moment of inertia tensor of the tile. The translational velocity \mathbf{u} and angular velocity $\boldsymbol{\omega}$ of the body can be found from \mathbf{a} and $\boldsymbol{\alpha}$ using a first order scheme as

$$\mathbf{u}^{t+\Delta t} = \mathbf{u}^t + \mathbf{a}^t \Delta t, \quad (4a)$$

$$\boldsymbol{\omega}^{t+\Delta t} = \boldsymbol{\omega}^t + \boldsymbol{\alpha}^t \Delta t. \quad (4b)$$

The superscript t in the above equations refers to the time at which these quantities are evaluated and Δt is the time step. By extension then, the new position \mathbf{x}_{cg} and orientation $\boldsymbol{\theta}$ of the tile are found using a similar first order scheme as

$$\mathbf{x}_{\text{cg}}^{t+\Delta t} = \mathbf{x}_{\text{cg}}^t + \mathbf{u}^{t+\Delta t} \Delta t, \quad (5a)$$

$$\boldsymbol{\theta}_{\text{cg}}^{t+\Delta t} = \boldsymbol{\theta}_{\text{cg}}^t + \boldsymbol{\omega}^{t+\Delta t} \Delta t. \quad (5b)$$

With the above set of equations, the motion of the tile in a moving fluid is determined as follows. At a given time step, the flow field in the chamber is solved using Eqs. (1) and (2) and the resulting linear and angular accelerations of the tile are calculated by integrating the total stress tensor over the tile surface via Eq. (3). The spatial and angular position of the tile is then updated using Eqs. (4) and (5). With the updated tile position the mesh surrounding the tile is updated and the process repeated until the tile reaches the target assembly site.

For the purpose of these simulations, we ignore the effect of gravity. As mentioned before, the chamber is such that $2H \ll L$; hence we can ignore flow in the z direction (i.e., $v_z = 0$). Given the large aspect ratio it is reasonable to assume that the flow within the chamber is parabolic with respect to the z direction (Poiseuille flow) and that any obstacles in the path of the flow will deflect it but not change this fundamental shape. There is flow above and below the tile; however, we can assume that this does not affect the flow along the sides of the tile and that the parabolic flow assumption is valid here.

For this system, the variation of flow with the z direction can be described as

$$v_x = v'_x \left(1 - \frac{z^2}{H^2}\right),$$

$$v_y = v'_y \left(1 - \frac{z^2}{H^2}\right),$$
(6)

where v'_x and v'_y are the peak velocities of the parabolic flow at the $z=0$ midplane. Since $v'_z=0$, the z momentum equation reduces to $\partial p / \partial z = 0$ and hence pressure does not vary with z .

With the above assumptions we can revise the x momentum equation by substituting Eq. (6) into Eq. (2) such that

$$\rho \left[\left(\frac{\partial v'_x}{\partial t} \left(1 - \frac{z^2}{H^2}\right) \right) + \left(v'_x \frac{\partial v'_x}{\partial x} + v'_y \frac{\partial v'_x}{\partial y} \right) \left(1 - \frac{z^2}{H^2}\right)^2 \right]$$

$$= - \frac{\partial p}{\partial x} + \mu \left(\frac{\partial^2 v'_x}{\partial x^2} + \frac{\partial^2 v'_x}{\partial y^2} \right) \left(1 - \frac{z^2}{H^2}\right) - 2\mu \frac{v'_x}{H^2},$$
(7)

which at $z=0$ reduces to

$$\rho \left(\frac{\partial v'_x}{\partial t} + v'_x \frac{\partial v'_x}{\partial x} + v'_y \frac{\partial v'_x}{\partial y} \right) = - \frac{\partial p}{\partial x} + \mu \left(\frac{\partial^2 v'_x}{\partial x^2} + \frac{\partial^2 v'_x}{\partial y^2} \right)$$

$$- 2\mu \frac{v'_x}{H^2}.$$
(8a)

Similarly, the y momentum equation can be written as

$$\rho \left(\frac{\partial v'_y}{\partial t} + v'_x \frac{\partial v'_y}{\partial x} + v'_y \frac{\partial v'_y}{\partial y} \right) = - \frac{\partial p}{\partial y} + \mu \left(\frac{\partial^2 v'_y}{\partial x^2} + \frac{\partial^2 v'_y}{\partial y^2} \right)$$

$$- 2\mu \frac{v'_y}{H^2}.$$
(8b)

Equations (8a) and (8b) represent the modified momentum equations that describe the flow in the midplane of the chamber. The flow structure specified by these equations is essentially 2D in nature, although the flow varies in all three dimensions. Solving for the full 3D Navier–Stokes equations described by Eq. (2) is computationally expensive, especially since our process of simulation requires the mesh to be updated at each time step as the tile moves through the fluid. Equations (8a) and (8b), on the other hand, describe our system in two dimensions while capturing the relevant 3D effects and reducing computational time in the process. The approach used to derive the above equations is similar to that used in classical lubrication theory³⁹ and in the modeling of flow in a Hele-Shaw cell.⁴⁰

Subject to the assumptions outlined above, it can be shown that the total linear force on the tile, \mathbf{F} , comprises of the summation of the pressure and shear forces acting on its sides (surface \mathbf{S}_1), \mathbf{F}_{p,S_1} and \mathbf{F}_{v,S_1} , respectively, and the shear forces on the upper and lower faces (surface \mathbf{S}_2), \mathbf{F}_{v,S_2} , resulting from the flow over and under the tile. Figure 2 shows the tile and its surfaces in detail. There is no pressure force on surface \mathbf{S}_2 since the pressure is invariant in the z direction. The torque on the tile can be expressed similarly, such that

$$\mathbf{F} = \mathbf{F}_{p,S_1} + \mathbf{F}_{v,S_1} + \mathbf{F}_{v,S_2},$$
(9a)

$$\mathbf{T} = \mathbf{T}_{p,S_1} + \mathbf{T}_{v,S_1} + \mathbf{T}_{v,S_2}.$$
(9b)

The pressure force \mathbf{F}_{p,S_1} is given by the integral of the pressure about the circumference of the tile via

$$\mathbf{F}_{p,S_1} = - \oint_{S_1} p(x,y) \mathbf{dS}_1$$

$$= - \oint_C p(x,y) \mathbf{n} dC \int_{-h}^h dz$$

$$= - 2h \oint_C p(x,y) \mathbf{n} dC,$$
(10a)

where S_1 is the surface area along the sides of the tile, \mathbf{dS}_1 is an area vector element on the side of the tile, $|\mathbf{dS}_1| = (dz) \times (dC)$ where dC is a length element along the circumference of the tile, dz is a length element along the z axis, \mathbf{n} is the normal along \mathbf{dS}_1 (Fig. 2), and $p(x,y)$ is the x - y pressure field. Similarly, the torque due to pressure, \mathbf{T}_{p,S_1} , on the sides of the tile is given by

$$\mathbf{T}_{p,S_1} = - \int_{S_1} \mathbf{r} \times p(x,y) \mathbf{dS}_1$$

$$= - \oint_C \mathbf{r} \times p(x,y) \mathbf{n} dC \int_{-h}^h dz$$

$$= - 2h \oint_C \mathbf{r} \times p(x,y) \mathbf{n} dC.$$
(10b)

The viscous force \mathbf{F}_{v,S_1} on the sides of the tile is given by

$$\mathbf{F}_{v,S_1} = \oint_{S_1} \boldsymbol{\tau} \cdot \mathbf{dS}_1 = \oint_{S_1} \mu \nabla \mathbf{v} \cdot \mathbf{n} |\mathbf{dS}_1|.$$
(11a)

Substituting Eq. (6) in the above equation, we have

$$\mathbf{F}_{v,S_1} = \mu \oint_{S_1} (\nabla \mathbf{v}' \cdot \mathbf{n}) \left(1 - \frac{z^2}{H^2}\right) |\mathbf{dS}_1|$$

$$= \mu \oint_C (\nabla \mathbf{v}' \cdot \mathbf{n}) dC \int_{-h}^h \left(1 - \frac{z^2}{H^2}\right) dz$$

$$= \beta (\mu \oint_C (\nabla \mathbf{v}' \cdot \mathbf{n}) dC),$$
(11b)

where

$$\beta = \int_{-h}^h \left(1 - \frac{z^2}{H^2}\right) dz.$$
(11c)

For instance, for a 30 μm tile ($h=15 \mu\text{m}$) in a 50 μm chamber ($H=25 \mu\text{m}$), $\beta=26.4 \mu\text{m}$.

Similarly, the viscous torque \mathbf{T}_{v,S_1} on the sides of the tile is given by

$$\mathbf{T}_{v,S_1} = \beta (\mu \oint_C \mathbf{r} \times (\nabla \mathbf{v}' \cdot \mathbf{n}) dC).$$
(11d)

As mentioned above, in addition to the force and torque on the sides of the tile, the flow above and below the tile exerts an additional shear force. We can separate the flow

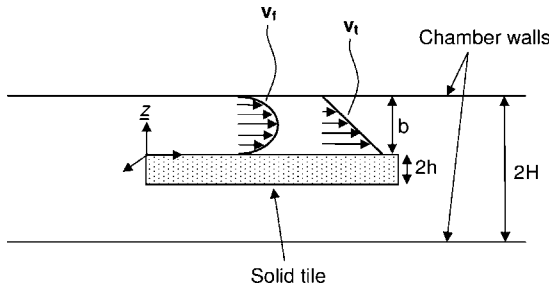


FIG. 3. Schematic showing flow above the tile and the coordinate system used to describe the flow.

field above and below the tile into two independent components. First, the flow field is affected by the fluid motion in the chamber which causes a flow velocity \mathbf{v}_f above and below the tile. Second, it is affected by the motion of the tile itself, which causes a flow velocity \mathbf{v}_t above and below the tile. Figure 3 is a schematic showing these velocities. Let $b = H - h$ be the free fluid space above or below the tile in the chamber and \underline{z} be the coordinate denoting distance from the tile surface to the chamber wall.

The \mathbf{v}_f component of fluid velocity will assume a parabolic shape because it is due to the pressure difference between the upstream and downstream ends to the tile. Let ∇p_t be the pressure drop per unit length across the top of the tile. Then the fluid flow is given by

$$\mathbf{v}_f = -\frac{b^2}{2\mu} \left(\frac{\underline{z}}{b} - \frac{\underline{z}^2}{b^2} \right) \nabla p_t. \quad (12a)$$

Similarly, the \mathbf{v}_t component of fluid velocity can be expressed as a Couette flow profile, with

$$\mathbf{v}_t = \mathbf{u}_{\text{tile}} \left(1 - \frac{\underline{z}}{b} \right), \quad (12b)$$

where \mathbf{u}_{tile} is the tile velocity. The net viscous force on the top and bottom tiles due to \mathbf{v}_f , $\mathbf{F}_{\mathbf{v},S_{2a}}$, is given by

$$\begin{aligned} \mathbf{F}_{\mathbf{v},S_{2a}} &= 2\mu \int_{S_2} \frac{\partial \mathbf{v}_f}{\partial \underline{z}} \Big|_{\underline{z}=0} |\mathbf{dS}_2| \\ &= -b^2 \int_{S_2} \frac{\partial}{\partial \underline{z}} \left(\frac{\underline{z}}{b} - \frac{\underline{z}^2}{b^2} \right) \Big|_{\underline{z}=0} \nabla p_t |\mathbf{dS}_2| \\ &= -b \int_{S_2} \nabla p_t |\mathbf{dS}_2| \\ &= \left(\frac{b}{2h} \right) \left(-2h \oint_C p(x,y) \mathbf{n} dC \right) \\ &= \mathbf{F}_{\mathbf{p},S_1} \left(\frac{b}{2h} \right), \end{aligned} \quad (13a)$$

where we have used the definition of $\mathbf{F}_{\mathbf{p},S_1}$ [Eq. (10a)]. We have used the divergence theorem here to convert the surface integral to an integral over the circumference of the tile.

Similarly, the net viscous force on the top and bottom tiles due to \mathbf{u}_{tile} , $\mathbf{F}_{\mathbf{v},S_{2b}}$, is given by

$$\mathbf{F}_{\mathbf{v},S_{2b}} = 2\mu \int_{S_2} \frac{\partial \mathbf{v}_t}{\partial \underline{z}} \Big|_{\underline{z}=0} |\mathbf{dS}_2| = -\frac{2\mu l^2 \mathbf{u}_{\text{tile}}}{b}. \quad (13b)$$

To calculate the viscous torque on the top and bottom of the tile, we use a slightly different approach. We consider the torque to be due to the fluid velocity, \mathbf{v}_f (similar to our previous approach), and due to the rotation of the tile, $\boldsymbol{\omega}_t$. The torque on the tile due to \mathbf{v}_f , $\mathbf{T}_{\mathbf{v},S_{2a}}$, is given by

$$\begin{aligned} \mathbf{T}_{\mathbf{v},S_{2a}} &= 2\mu \int_{S_2} \mathbf{r} \times \frac{\partial \mathbf{v}_f}{\partial \underline{z}} \Big|_{\underline{z}=0} |\mathbf{dS}_2| \\ &= -b \int_{S_2} \mathbf{r} \times \nabla p_t |\mathbf{dS}_2| \\ &= \mathbf{T}_{\mathbf{p},S_1} \left(\frac{b}{2h} \right), \end{aligned} \quad (14a)$$

where $\mathbf{T}_{\mathbf{p},S_1}$ is defined in Eq. (10b). Again, we have used the divergence theorem to convert the surface integral to an integral over the tile boundary.

The torque due to the rotation of the tile can be found by assuming that the tile is a disk of radius R ($R = l / \sqrt{\pi}$). The velocity profile at a point on the tile with radius r is given by

$$\mathbf{v}_t = \boldsymbol{\omega}_{\text{tile}} \times \mathbf{r} \left(1 - \frac{\underline{z}}{b} \right). \quad (14b)$$

The torque due to the rotation of the tile, $\mathbf{T}_{\mathbf{v},S_{2b}}$, is therefore given by

$$\begin{aligned} \mathbf{T}_{\mathbf{v},S_{2b}} &= 2\mu \int_{S_2} \mathbf{r} \times \frac{\partial \mathbf{v}_t}{\partial \underline{z}} \Big|_{\underline{z}=0} |\mathbf{dS}_2| \\ &= -\frac{2\mu}{b} \int_0^{2\pi} \int_0^R \mathbf{r} \times (\boldsymbol{\omega}_{\text{tile}} \times \mathbf{r}) r dr d\theta \\ &= -\frac{4\mu\pi}{b} \int_0^R \mathbf{r} \times (\boldsymbol{\omega}_{\text{tile}} \times \mathbf{r}) r dr \\ &= -\frac{\mu\pi \boldsymbol{\omega}_{\text{tile}} R^4}{b}. \end{aligned} \quad (14c)$$

Finally, the net force and torque on the tile are given by

$$\begin{aligned} \mathbf{F} &= -2h \oint_C p(x,y) \mathbf{n} dC + \mu\beta \oint_C (\nabla \mathbf{v}' \cdot \mathbf{n}) dC + \mathbf{F}_{\mathbf{p},S_1} \left(\frac{b}{2h} \right) \\ &\quad - \frac{2\mu l^2 \mathbf{u}_{\text{tile}}}{b}, \end{aligned} \quad (15a)$$

$$\begin{aligned} \mathbf{T} &= -2h \oint_C \mathbf{r} \times p(x,y) \mathbf{n} dC \\ &\quad + \mu\beta \oint_C \mathbf{r} \times (\nabla \mathbf{v}' \cdot \mathbf{n}) dC + \mathbf{T}_{\mathbf{p},S_1} \left(\frac{b}{2h} \right) - \frac{\mu\pi \boldsymbol{\omega}_{\text{tile}} R^4}{b}. \end{aligned} \quad (15b)$$

TABLE I. Summary of forces and torque experienced by a solid tile in a fluidic chamber.

		Force	Torque
Tile sides	Due to pressure	$\mathbf{F}_{p,S_1} = -2h\phi_C p(x,y)\mathbf{n}dC$	$\mathbf{T}_{p,S_1} = -2h\phi_C \mathbf{r} \times p(x,y)\mathbf{n}dC$
	Due to viscosity	$\mathbf{F}_{v,S_1} = \mu\beta\phi_C (\nabla\mathbf{v}' \cdot \mathbf{n})dC$	$\mathbf{T}_{v,S_1} = \mu\beta\phi_C \mathbf{r} \times (\nabla\mathbf{v}' \cdot \mathbf{n})dC$
Top and bottom of tile	Due to fluid velocity	$\mathbf{F}_{v,S_{2a}} = \mathbf{F}_{p,S_1}(b/2h)$	$\mathbf{T}_{v,S_{2a}} = \mathbf{T}_{p,S_1}(b/2h)$
	Due to tile velocity	$\mathbf{F}_{v,S_{2b}} = -2\mu l^2 \mathbf{u}_{\text{tile}}/b$	$\mathbf{T}_{v,S_{2b}} = -\mu\pi\omega_{\text{tile}}R^4/b$

In order to model our system in 2D simulations, we solve the modified Navier–Stokes equations, Eqs. (8a) and (8b). Instead of using Eqs. (3a) and (3) to update the tile position, we use Eqs. (15a) and (15b). The rest of the simulation procedure remains the same as previously discussed. The forces on the tile are summarized in Table I.

III. VALIDATION OF 2D MODEL

In order to validate the above 2D model, we compared the results of our 2D simulations with 3D simulations, as well as with experimental results. For the numerical validation we carried out steady 2D and 3D simulations for different tile thicknesses, positions, inlet velocities, and tile velocities and compared the pressure and viscous force exerted on the tile. The simulations were carried out using the commercial software FLUENT, with the modified x and y momentum equations given by Eqs. (8a) and (8b) and the modified force and torque terms on the tile given by Eqs. (15a) and (15b). In

all cases grid independence studies were performed to ensure that mesh density was sufficient.

In these simulations tiles with $l=500 \mu\text{m}$ and $2h=30, 45, \text{ and } 50 \mu\text{m}$ were used in a chamber of dimensions of $3 \text{ mm} \times 5 \text{ mm} \times 50 \mu\text{m}$. The fluid flow was such that the upper part of the chamber acted as an inlet, while the lower part of the chamber acted as an outlet as shown in Figs. 4(a) and 4(c). Three cases were considered with midplane inlet velocities of $V_{2D} = -1.5 \times 10^{-2}, -1.5 \times 10^{-3}, \text{ and } -1.5 \times 10^{-4} \text{ m/s}$, which corresponded to the peak velocities for the corresponding 3D simulations which had a parabolic inlet profile.

Simulations were carried out with no tile velocity, as well as ascribed translational and rotational tile velocities. In the case of translational velocity, we ascribed a tile velocity $\mathbf{u}_{\text{tile}} = 10^{-3} \text{ m/s}$ in the y direction and positioned the tile as shown in Fig. 4(a) (scheme I), while for the rotating tile, we set the tile angular velocity $\omega_{\text{tile}} = 10^{-2} \text{ rad/s}$ in the z direc-

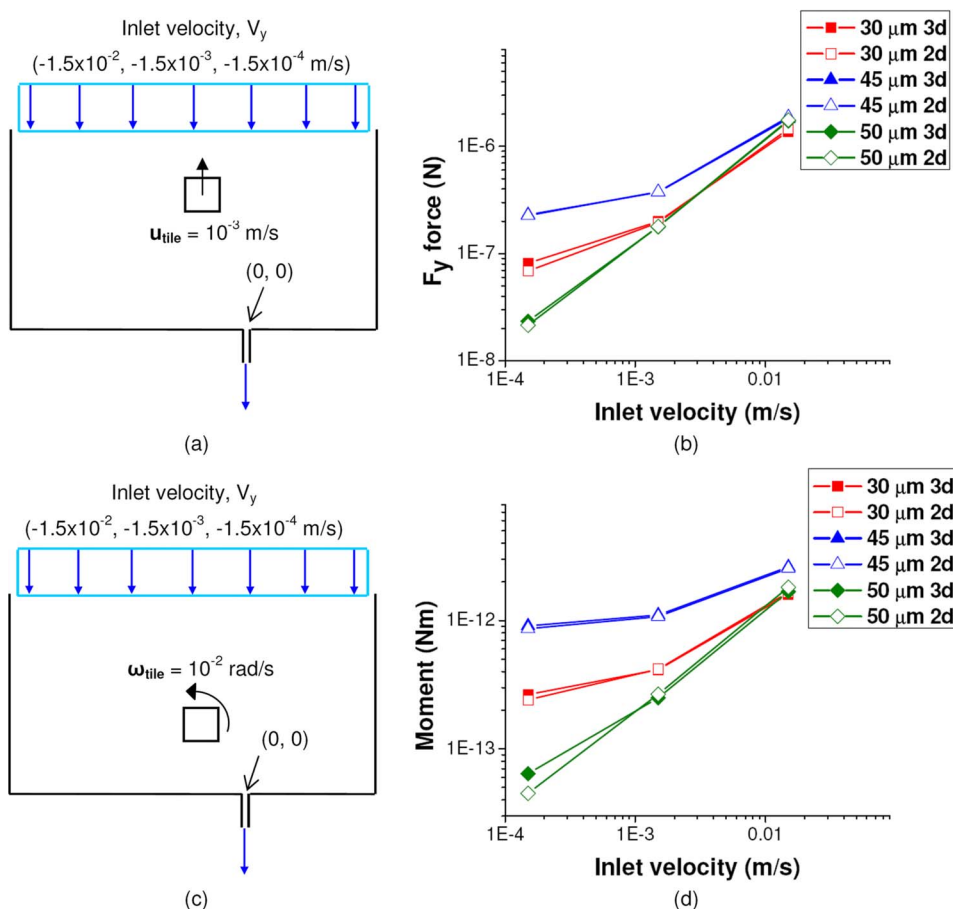


FIG. 4. (Color online) Comparison of 2D and 3D steady state simulations. (a) Scheme I: Tile position is $(-250 \mu\text{m}, 2500 \mu\text{m})$, and a translational velocity $u_{\text{tile}} = 10^{-3} \text{ m/s}$ was added to the tile. (b) shows the variation in F_y force with fluid velocity for scheme I. (c) Scheme II: Tile position is $(-250 \mu\text{m}, 1000 \mu\text{m})$, and a rotational velocity $\omega_{\text{tile}} = 10^{-2} \text{ rad/s}$ was added to the tile. (d) shows the variation in torque with fluid velocity for scheme II.

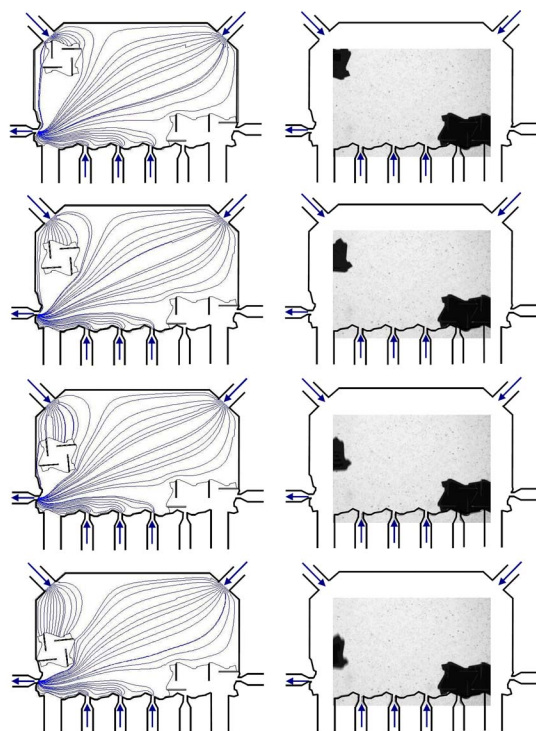


FIG. 5. (Color online) Comparison of 2D simulations and experiments. The left column shows tile movement through a microfluidic chamber in simulation and the right in experiment. The arrows indicate the fluid inlets and outlets in the system.

tion and the position of the tile to that in Fig. 4(c) (scheme II). Figures 4(b) and 4(d) show the results of our simulations for the translational and rotational velocity cases, where we have compared the force and torque on the tile for the 2D and 3D simulations. The results of our 2D and 3D simulations were found to match within 1%–7%, validating the 2D model.

The quantitative matching between our 2D and 3D simulations indicates that our model is physically accurate. A comparison of our 2D model with the experiments described by Tolley *et al.*²² also allowed us to obtain qualitative matching with experimental results. The assembling components were $500 \times 500 \times 30 \mu\text{m}^3$ silicon tiles with a passive latch on each side. The flow of fluid in the experimental system was established using pressure driven flow. Our simulations modeled the tile motion in the microchamber, and we compared the path of a tile brought down from the top of the chamber to the bottom in experiment and in simulation. Figure 5 shows the results of this comparison. The images show the passage of the tile from the top left part of the chamber to the bottom. The results from the experiments show a smaller field of view than the whole assembly chamber because of the magnification used while imaging the experiment. The arrows in the figure indicate regions where flow enters and leaves the chamber. Comparison of the path of the tile in experiment and simulation visually indicates a rough qualitative matching between the two results. Given the quantitative agreement between the 2D and 3D numerical results and the qualitative matching between the 2D model and the experimental results, the model was considered physically accurate and used for the remaining simulations.

IV. RESULTS AND DISCUSSION

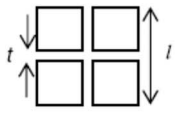
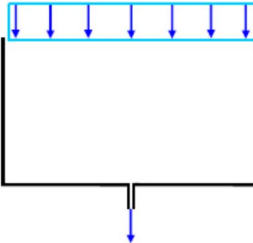
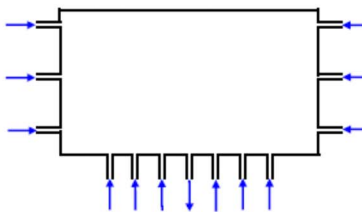
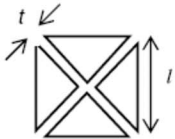
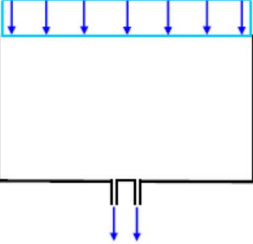
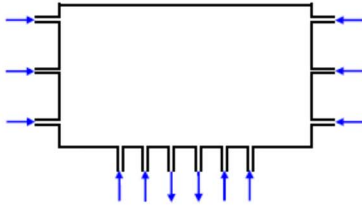
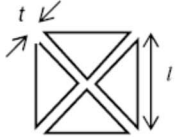
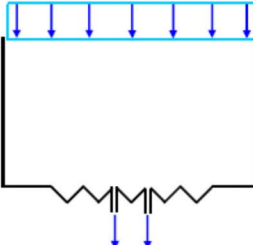
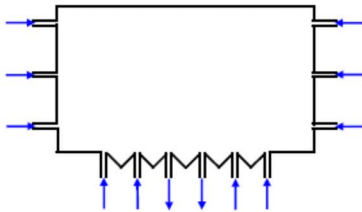

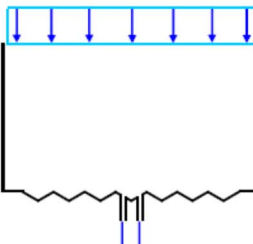
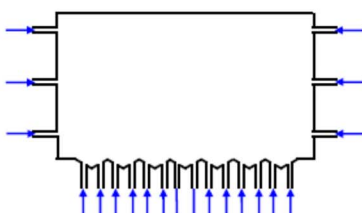
The goal of this paper was to use the model developed above to study the effect of tile shape, chamber geometry, and flow conditions on the efficiency of the assembly process. As mentioned previously, in an actual system we assume that tile motion far away from the attraction point is stochastic and hence the initial position and orientation of a tile are not determinable prior to assembly. We would therefore like to design an assembly scheme where successful assembly events occur over the broadest range of initial tile conditions. In order to do this, we considered numerous different assembly schemes and quantitatively evaluated them over a range of initial tile conditions using two docking parameters, as described below.

A. Simulation conditions

Figure 5 shows the assembly chamber used in our experimental system. The experimental assembly chamber had inlets along the bottom and sides of the chamber, a single outlet port, and a shape-matched, angled substrate where assembly occurred. The chamber design and flow patterns examined in simulation were different from those used in experiments though the overall chamber and tile dimensions were similar. For our simulations, we consider the different tile shapes, assembly chamber designs, and flow fields listed in Table II. The simulation assembly schemes were chosen to study different aspects of the DHFSA process including the design of inlet and outlet ports, substrate design, and tile shapes. The arrows in the assembly scheme figures indicate regions where flow enters and leaves the assembly chamber. We considered two tile shapes, namely, squares (Table II, schemes A1, A2, B1, B2, C1, and C2) and regular hexagons (Table II, schemes D1 and D2) with channels through them. The pattern of channels in the tile is based on the outlet configuration in the chamber to allow for subsequent assembly around a tile that has previously been assembled on the substrate. The final position of the tile will depend on flow conditions such as the inlet flow pattern in the chamber and the configuration of the outlet. We looked at two different inlet flow configurations in our simulations. The first consisted of flow entering the chamber from a single large inlet directly above the flow outlet in the chamber (Table II, schemes A1, B1, C1, and D1). The second consisted of flow entering the chamber from numerous side inlets located orthogonal as well as in line with the main flow outlet (Table II, schemes A2, B2, C2, and D2). The reason for considering these two inlet schemes was to examine the effects of both a vertical inlet configuration and a horizontal inlet configuration. Additionally, we also looked at different outlet configurations, namely, a single port outlet on a flat substrate (Table II, schemes A1 and A2), a dual port outlet on a flat substrate (Table II, schemes B1 and B2), and a dual port outlet on an angled, shape-matched substrate (Table II, schemes C1, C2, D1, and D2).

In all the cases, the tile being assembled was a silicon tile in water, with length $l \sim 500 \mu\text{m}$ and thickness $2h = 30 \mu\text{m}$ in a chamber of dimensions of $6l \times 10l \times 0.1l$ ($3 \text{ mm} \times 5 \text{ mm} \times 50 \mu\text{m}$). The peak inlet velocity into the

TABLE II. Different assembly schemes used for simulations.

Tile shape	Chamber Designs	
 <p>$t = 50\mu\text{m}, l = 500\mu\text{m}$</p>	 <p>Scheme A1</p>	 <p>Scheme A2</p>
 <p>$t = 50\mu\text{m}, l = 500\mu\text{m}$</p>	 <p>Scheme B1</p>	 <p>Scheme B2</p>
 <p>$t = 50\mu\text{m}, l = 500\mu\text{m}$</p>	 <p>Scheme C1</p>	 <p>Scheme C2</p>
 <p>$t = 50\mu\text{m}, l = 500\mu\text{m}$</p>	 <p>Scheme D1</p>	 <p>Scheme D2</p>

large single inlet port used in schemes A1, B1, C1, and D1 was $V = 1.5 \times 10^{-3}$ m/s, while the inlet velocity used in schemes A2, B2, C2, and D2 was $V = 1.5 \times 10^{-2}$ m/s. These values were chosen to minimize the time needed to carry out the simulations, but the velocity did not affect the path of the tile since the fluid regime is Stokesian for the velocities we considered. Additionally, the magnitude of these velocities was of the order of the velocities obtained in the experiments described previously, as determined by flow visualization methods.

In order to evaluate the assembly schemes, we considered a range of initial tile conditions which were defined by two angles of rotation, φ and ψ (Fig. 6). The angle φ refers to different tile positions spaced radially from the center of the chamber at angles of 0° , 15° , and 30° . The angle ψ refers to the initial tile orientation, given by the rotation of the tile

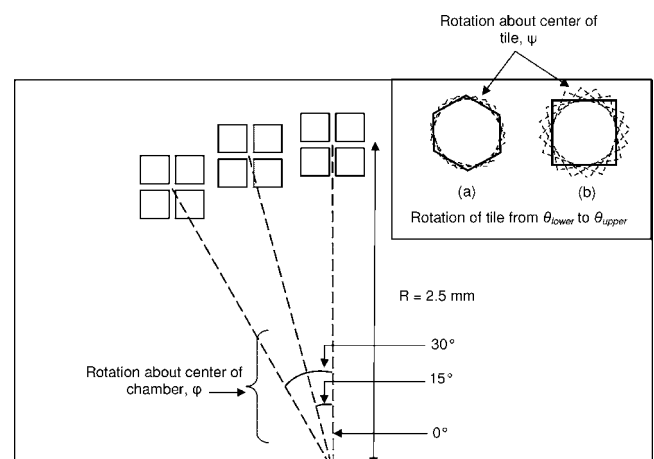


FIG. 6. Schematic showing different tile positions and orientations used for simulations. The chamber and tile shapes are representative of all the shapes listed in Table II.

about its own center of gravity. We looked at initial tile angles ranging from $\theta_{\text{lower}}=-45^\circ$ to $\theta_{\text{upper}}=45^\circ$ for square shaped tiles and from $\theta_{\text{lower}}=-30^\circ$ to $\theta_{\text{upper}}=30^\circ$ for hexagonal shaped tiles, which represent the range of unique tile orientations for these tile shapes.

A tile positioned directly above the outlet ($\varphi=0^\circ$) is expected to show the same assembly patterns for tile orientations symmetric with respect to the $\psi=0^\circ$ tile orientation. This is because the tile experiences a symmetric flow field at this position for all the assembly schemes studied. However, as the tile position moves away from the outlet ($\varphi=15^\circ, 30^\circ$), the tile experiences an asymmetric flow field with changing ψ , and hence assembly patterns are not expected to be symmetric with respect to the $\psi=0^\circ$ orientation. Therefore, although the target locations studied here were always along the centerline of the assembly chamber, the range of tile orientations and positions examined introduced asymmetric assembly patterns in our system, which could otherwise have been obtained by using target locations that were asymmetric with respect to the centerline of the chamber.

B. Docking parameters

Successful assembly of a tile on the substrate requires the orientation and position of the tile to match with those of the target substrate on assembly. In order to quantify the successful assembly of the tile, we have defined two docking parameters, $D_{x,y}$, which is the ‘‘translational docking parameter,’’ and D_θ , which is the ‘‘rotational docking parameter.’’ The assembly schemes considered here deal with the fluidic aspect of assembly, and our simulations do not account for any shape matching or collisions that can occur at the time of assembly. The docking parameters are therefore evaluated when the tile first touches the substrate, after which shape matching and collisions would control the final assembly process. If x and y are the positions of the center of gravity of the tile at the time of assembly and θ is the orientation of the tile, then we define the docking parameters as

$$D_{x,y} = \frac{\sqrt{(x-x_0)^2 + (y-y_0)^2}}{l}, \quad (16a)$$

$$D_\theta = \frac{|\theta - \theta_0|}{\theta_{\text{upper}} - \theta_{\text{lower}}}, \quad (16b)$$

where x_0 and y_0 are the coordinates of the center of gravity of the tile at the intended assembly position, θ_0 is the final orientation of the tile at this position, and l is the tile dimension. The docking parameter $D_{x,y}$ represents the translation a tile needs to undergo in order for it to be seated at the correct target location, while the docking parameter D_θ represents the rotation the tile needs to undergo for it to be correctly docked. $D_{x,y}$ has been nondimensionalized with respect to the tile length l , while D_θ has been nondimensionalized with respect to the maximum rotation a tile needs to undergo to return to its initial orientation [i.e., $(\theta_{\text{upper}} - \theta_{\text{lower}})$]. This is dependent on the tile shape: For instance, for a square tile, this angle is 90° , for a hexagonal tile, it is 60° , and for an irregularly shaped tile, it could be 360° .

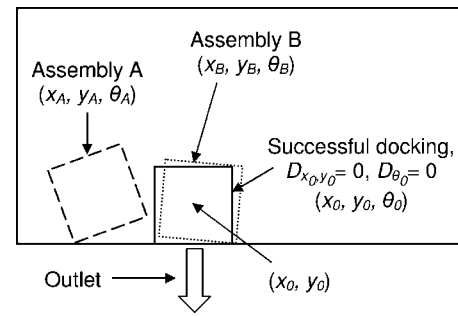


FIG. 7. Schematic showing different tile positions and orientations (x, y, θ) at the end of assembly. Assembly B shows better tile docking compared to assembly A; therefore $D_{x_B, y_B} \rightarrow D_{x_0, y_0} (=0)$ and $D_{\theta_B} \rightarrow D_{\theta_0} (=0)$, while $D_{x_A, y_A}, D_{\theta_A} > 0$.

In the limit of successful assembly, the final positions and orientations of the tile match those of the intended tile position and orientation (i.e., $x=x_0$, $y=y_0$, and $\theta=\theta_0$) and hence we have

$$\lim_{\substack{D_{x,y} \rightarrow D_{x_0, y_0} \\ x \rightarrow x_0 \\ y \rightarrow y_0}} D_{x,y} = \lim_{\substack{x \rightarrow x_0 \\ y \rightarrow y_0}} \frac{\sqrt{(x-x_0)^2 + (y-y_0)^2}}{l} = 0, \quad (17a)$$

$$\lim_{D_\theta \rightarrow D_{\theta_0}} D_\theta = \lim_{\theta \rightarrow \theta_0} \frac{|\theta - \theta_0|}{\theta_{\text{upper}} - \theta_{\text{lower}}} = 0. \quad (17b)$$

For all other cases, $D_{x,y} > 0$ and $D_\theta > 0$, since $x \neq x_0$, $y \neq y_0$, and $\theta \neq \theta_0$. A theoretical upper bound can be obtained for $D_{x,y}$ and D_θ in the following manner. For $D_{x,y}$, the maximum value of the numerator is given by the maximum chamber dimension which is $\sim L$. Therefore $\max(D_{x,y}) \sim L/l \gg 0$. For D_θ , the maximum value of the numerator is $(\theta_{\text{upper}} - \theta_{\text{lower}})/2$, and hence $\max(D_\theta) = 0.5$.

Figure 7 compares the final tile location of a successfully assembled tile with those of tiles assembled by two other schemes, assembly A and assembly B. From the figure we see that the tile location at the end of assembly B is closer to the tile location at successful assembly as compared to the tile in assembly A. As a result, the docking parameter values for the tile in assembly B are closer to zero in value than for those in the tile in assembly A. The docking parameters are thus a means by which to compare different assembly schemes, though the comparison must take place across different initial tile conditions rather than for a single case of assembly. A scheme which gives $D_{x,y} \sim 0$ and $D_\theta \sim 0$ for most initial tile positions is better than a scheme where $D_{x,y}$ and $D_\theta \gg 0$ for most cases of assembly. The docking parameters do not give us an absolute measure of successful assembly, and it is not possible to predict the range of docking parameter values that indicate successful assembly. This is because other factors such as final shape matching between tile and substrate and the nature of the collision occurring also have an effect on the final assembly process. Rather, the docking parameters serve as a means of comparing the probability of successful assembly occurring for different assembly schemes. To summarize, the lower the docking parameter values for a given assembly process across different initial

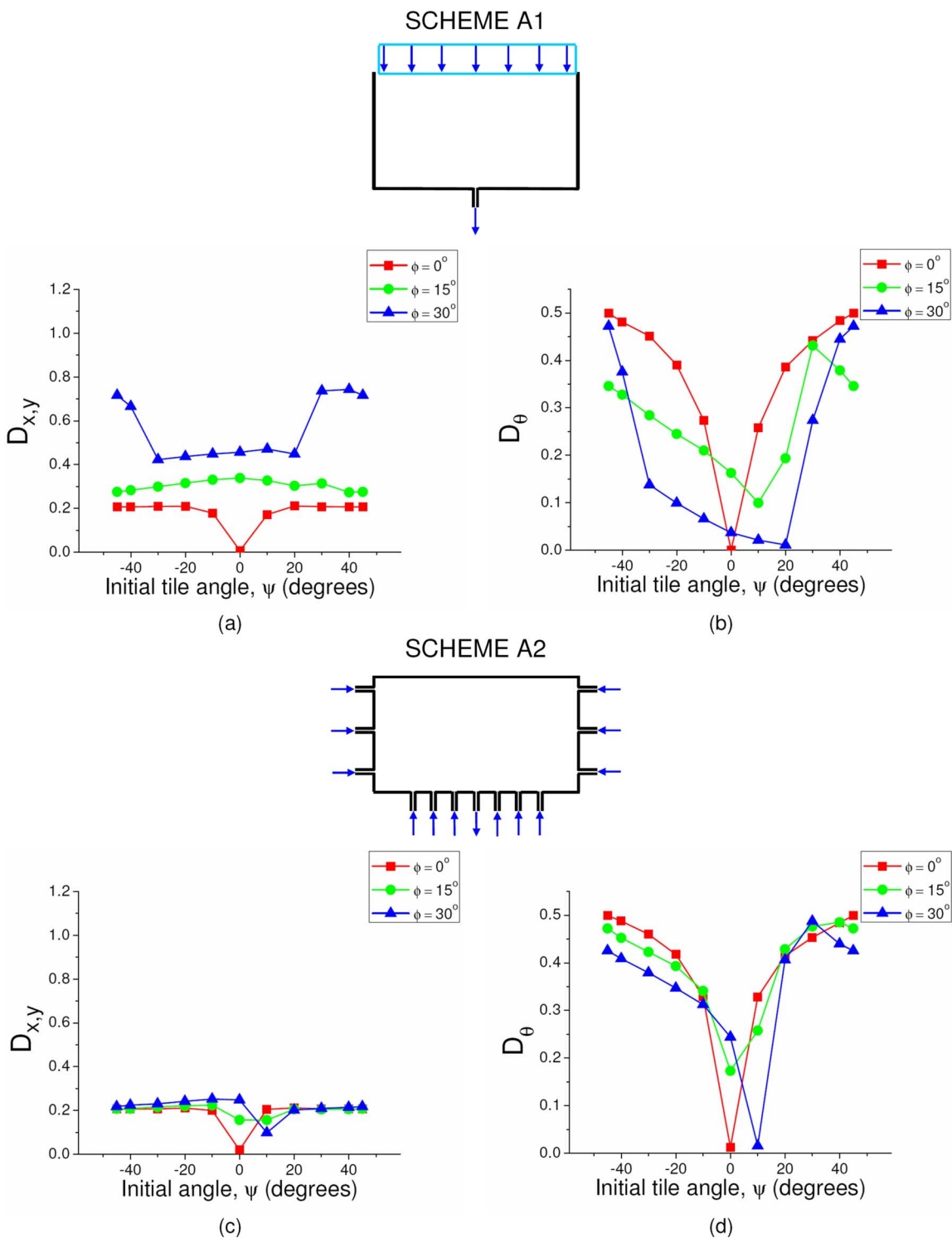


FIG. 8. (Color online) $D_{x,y}$ and D_{θ} for schemes A1 and A2: [(a) and (b)] scheme A1; [(c) and (d)] scheme A2.

tile conditions, the more likely it is that the process leads to successful assembly. The above docking parameters were used to compare the different assembly procedures listed in Table II for various initial tile configurations as discussed below.

The results of our simulations for the different assembly schemes considered are shown in Figs. 8–11. The graphs in these figures show the variation in $D_{x,y}$ and D_{θ} with initial tile angles for the different assembly schemes. Figure 8

shows the results for assembly schemes A1 and A2, Fig. 9 shows the results for schemes B1 and B2, Fig. 10 shows the results for schemes C1 and C2, and Fig. 11 shows the results for schemes D1 and D2. The variation in the two docking parameters is shown as a function of initial tile orientation ψ for each of the three tile positions given by angle ϕ . The effect of the inlet flow patterns and the different outlet configurations on tile assembly is discussed in more detail in Secs. IV C and IV D.

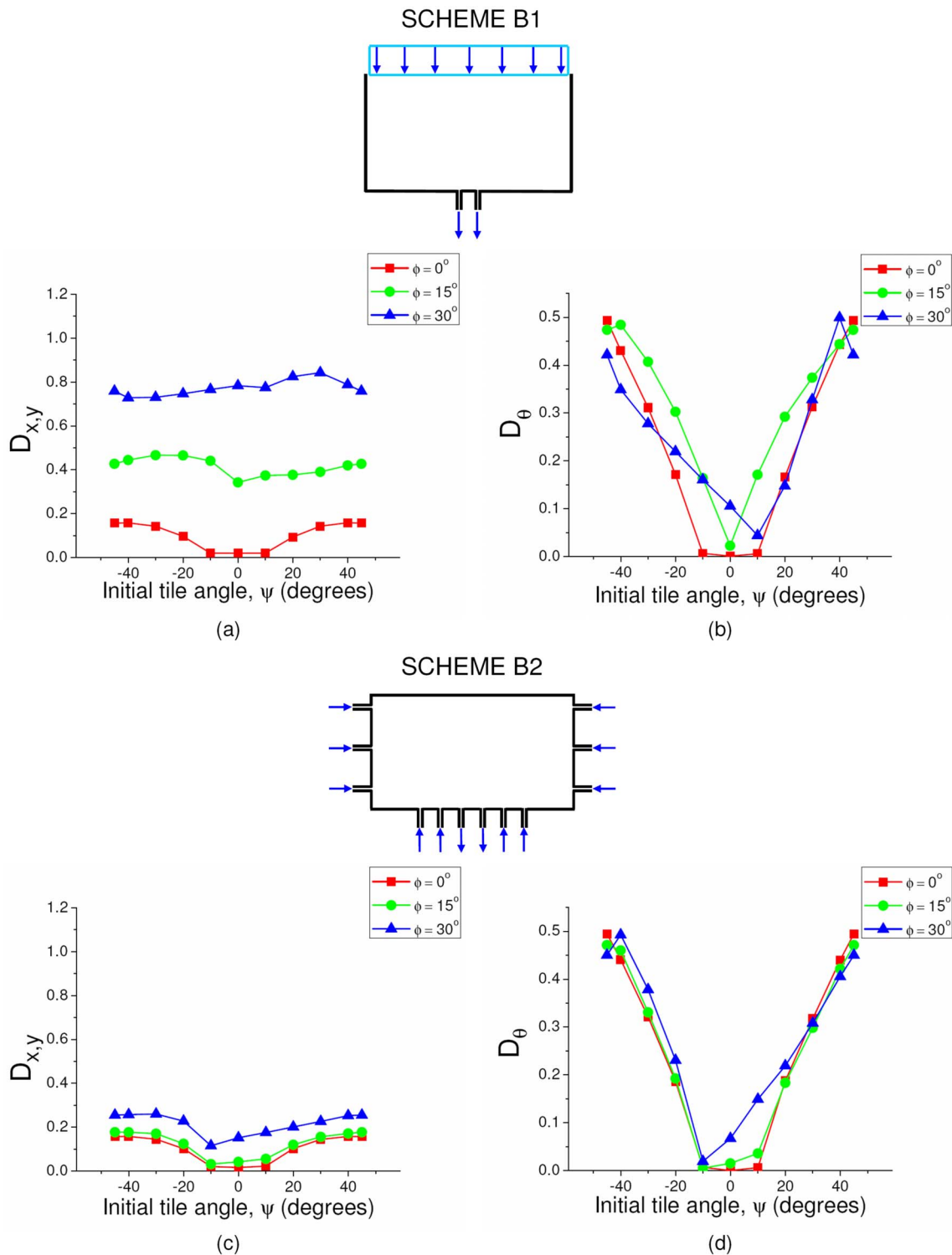


FIG. 9. (Color online) $D_{x,y}$ and D_θ for schemes B1 and B2: [(a) and (b)] scheme B1; [(c) and (d)] scheme B2.

C. Effect of inlet flow patterns

As mentioned previously, we considered two different inlet flow patterns as shown in Table II, the first consisting of flow entering the chamber from a single top inlet directly above the flow outlet in the chamber (schemes A1, B1, C1, and D1) and the second consisting of flow entering the chamber from numerous side inlets (schemes A2, B2, C2, and D2). For a tile positioned directly above the outlet (ϕ

$=0^\circ$), it is seen that the two docking parameters are symmetric about a 0° initial tile orientation ($\psi=0^\circ$) for all the assembly schemes, as expected.

More generally, the schemes which had flow coming in from multiple side inlets (schemes A2, B2, C2, and D2) were found to have significantly lower values of the translational docking parameter, $D_{x,y}$ [Figs. 8(c), 9(c), 10(c), and 11(c)], for different tile positions, as compared to the other schemes

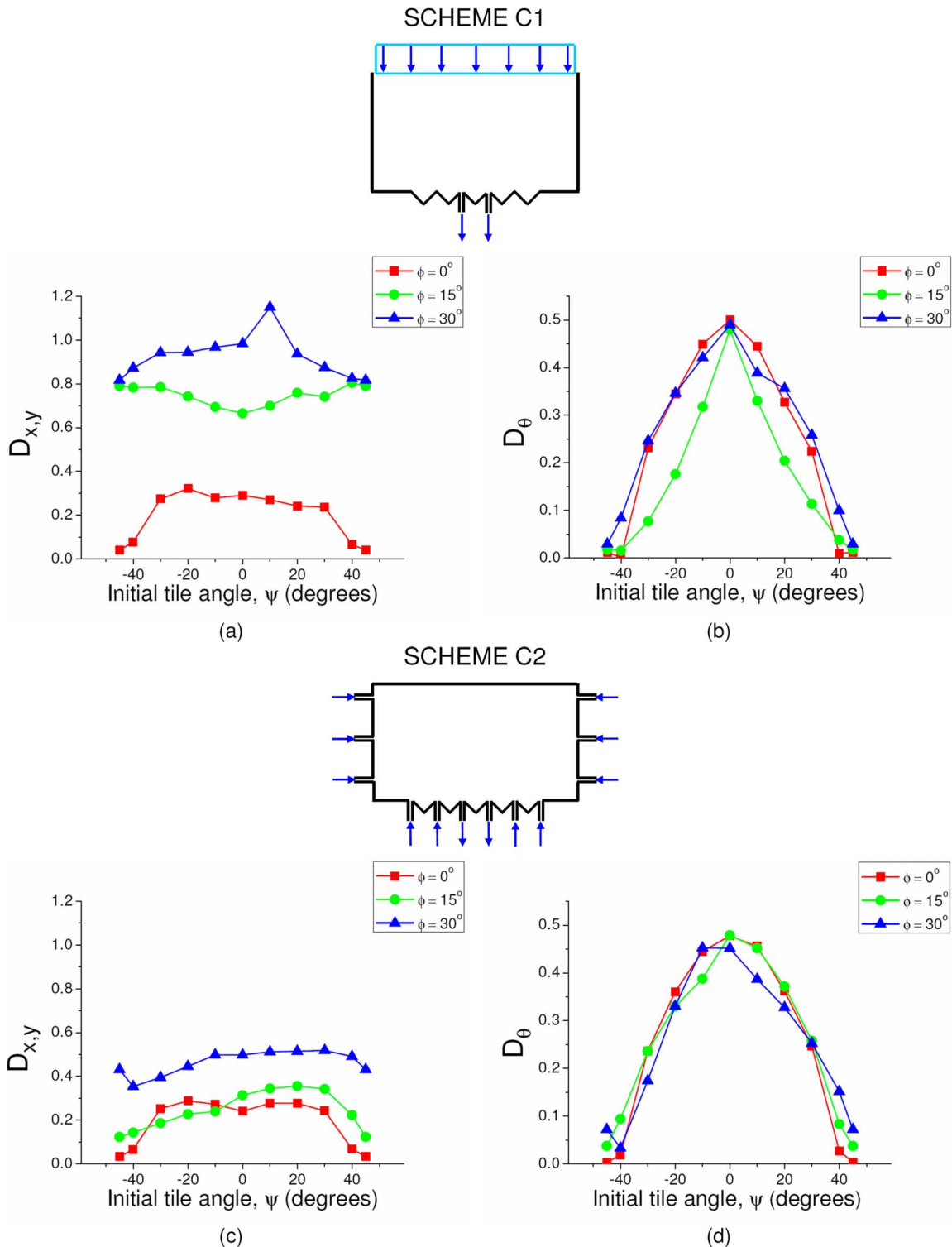


FIG. 10. (Color online) $D_{x,y}$ and D_θ for schemes C1 and C2: [(a) and (b)] scheme C1; [(c) and (d)] scheme C2.

where flow only entered the chamber from a single top inlet (schemes A1, B1, C1, and D1) which had much higher values of $D_{x,y}$ [Figs. 8(a), 9(a), 10(a), and 11(a)]. Although the latter schemes showed low values of $D_{x,y}$ when the tile was positioned directly above the outlet, the $D_{x,y}$ values were found to dramatically increase with increasing ϕ , indicating deteriorating assembly as the tile moved its position away from the center of the chamber. For instance, the $D_{x,y}$ param-

eter had a maximum value of 0.25 for the A2 assembly scheme with the side inlets [Fig. 8(c)], while it had a maximum value as high as 0.74 for the A1 assembly scheme with the single top inlet [Fig. 8(a)]. The effect of the side inlets was, however, more significant on the $D_{x,y}$ docking parameter than on the D_θ parameter. As such, no significant trends were observed for the rotational docking parameter, D_θ , for the different inlet flow configurations.

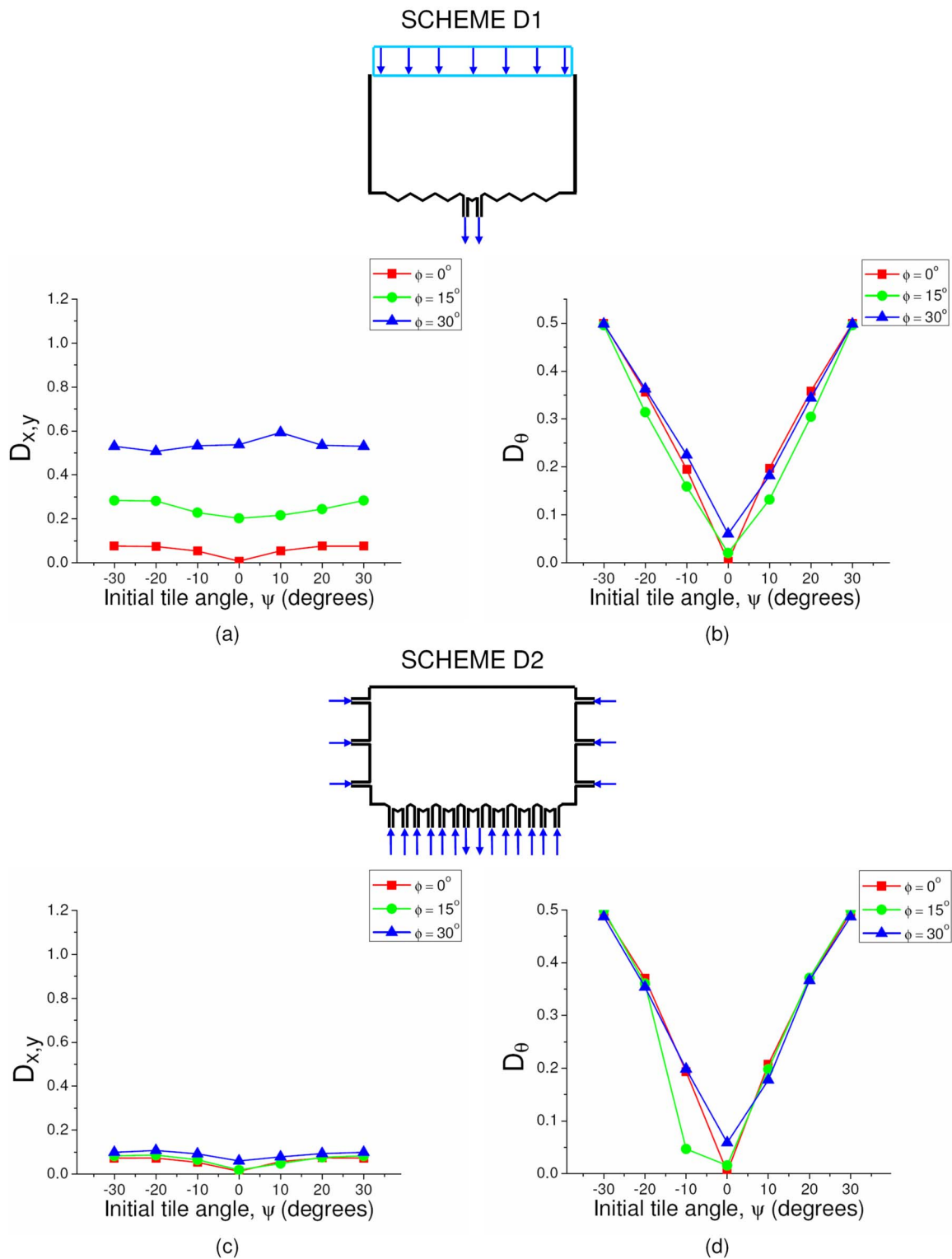


FIG. 11. (Color online) $D_{x,y}$ and D_θ for schemes D1 and D2: [(a) and (b)] scheme D1; [(c) and (d)] scheme D2.

D. Effect of outlet configuration

Different outlet configurations were studied using the assembly schemes listed in Table II, namely, a single port outlet on a flat substrate (schemes A1 and A2), a dual port outlet on a flat substrate (schemes B1 and B2), and a dual port outlet on an angled, shape-matched substrate (schemes C1, C2, D1, and D2). For a tile positioned directly above the

outlet, the effect of a dual outlet port on a square tile was to cause a tile having an initial tile orientation close to 0° ($\psi \sim 0^\circ$) to assemble on a substrate at a final angle approaching 0° . This effect is observed in the relatively flat profiles of the D_θ graphs for these schemes near initial tile angles of 0° for $\phi = 0^\circ$ [Figs. 9(b), 9(d), 10(b), and 10(d)]. The effect of the single outlet port, however, was to cause a square tile having

an initial tile orientation close to 45° ($\psi \sim 45^\circ$) to assemble on a substrate at a final angle approaching 45° , which can be seen in the relatively flat profiles of the relevant D_θ graphs near initial tile angles of 45° , for $\varphi=0^\circ$ [Figs. 8(b) and 8(d)]. Hence it was found that a single port outlet configuration tended to rotate a square tile to a 45° final angle when possible, while a dual port outlet configuration tended to rotate a tile to a 0° final angle. This indicates that a single port outlet is useful for assembly of a square tile on an angled substrate, while a dual port outlet is useful for assembly on a flat substrate.

By contrast, for the hexagonal tile, the strongly linear profiles of the D_θ graphs indicates that the fluid flow does not significantly rotate the tile as it moves toward the outlet. Thus the tile orientation at assembly is similar to the initial orientation of the tile [Figs. 11(b) and 11(d)]. Therefore the dual outlet configuration only has a significant effect on the rotation of a square tile, while it does not tend to change the orientation of a hexagonal tile.

E. Effect of tile shape

Two different tile shapes were studied in these simulations, namely, a square tile shape (schemes A1, A2, B1, B2, C1, and C2) and a hexagonal tile shape (schemes D1 and D2). By comparing Figs. 8–10, which show the variation in the docking parameters for square tiles, with Fig. 11, which shows the same for hexagonal tiles, the following results may be observed. First, the values of the translational docking parameter, $D_{x,y}$, for different initial tile positions and orientations tended to be lower for the hexagonal tile shape, indicating that the hexagonal tile performed better than the square tile in terms of translational docking. However, upon comparing the rotational docking parameter, D_θ , it was found that the hexagonal tile did not undergo significant rotation due to the flow field, as discussed previously. This lack of rotation is probably due to the increased number of sides in a hexagonal tile as compared to a square tile and could be useful in designing future assembly schemes where an alternative method that does not directly involve the use of fluid motion (such as using the shape of the hexagon) is used to deterministically control the initial orientation of a hexagonal tile upstream of the assembly site. Subsequently, fluid flow can be used to transport and assemble the tile at the desired location without changing its orientation.

Figures 12 and 13 show tile locations as a function of time for tiles having initial orientations $\psi=45^\circ$ (for square tiles) and $\psi=30^\circ$ (for hexagonal tiles) and initial position $\varphi=30^\circ$. The black outline squares and hexagons indicate the target tile locations while the arrows indicate fluid outlets. The flow lines shown here are pathlines, and the effect of multiple side inlets on the final tile position and orientation can be clearly seen here. Figure 12 shows the path of a tile moving through the chamber with a single top inlet (schemes A1, B1, C1, and D1), while Fig. 13 shows the path of a tile moving through the chamber with multiple side inlets (schemes A2, B2, C2, and D2), with the images showing the variation in the tile position with time as the assembly process progresses. We can characterize the time taken for a tile

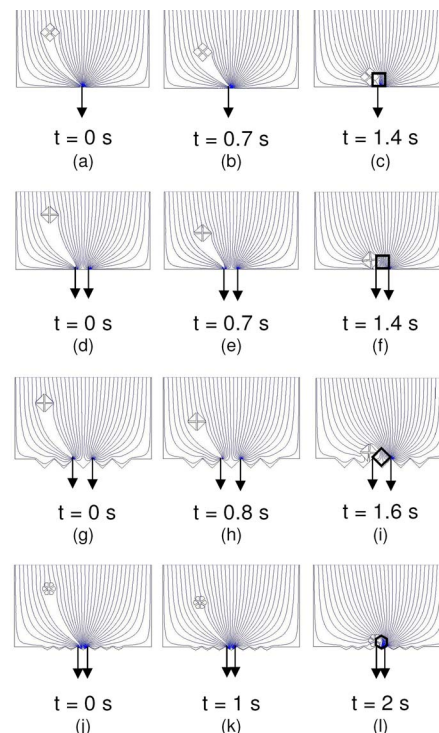


FIG. 12. (Color online) Time elapsed images showing tile locations for tiles with initial orientation $\psi=45^\circ/30^\circ$ and initial position $\varphi=30^\circ$: [(a)–(c)] scheme A1; [(d)–(f)] scheme B1; [(g)–(i)] scheme C1; [(j)–(l)] scheme D1. The black outlined squares and hexagons indicate the target tile locations, while the arrows indicate fluid outlets.

to assemble by defining a nondimensional time constant for the assembly process as $t_0=l/V$. Then, the time it took for tiles to assemble was found to be between $4t_0$ and $6t_0$ for the schemes with a single top inlet (schemes A1, B1, C1, and D1) with $t_0=0.333$ s. Similarly for the schemes with multiple side inlets (schemes A2, B2, C2, and D2) with $t_0=0.0333$ s, assembly time was found to be between $40t_0$ and $60t_0$. The images in the above figures show the tile position at the beginning, halfway through, and at the end of the assembly. Multiple side inlets are seen to improve the translational docking of the tile, placing the tile nearer the final target location as compared to a single top inlet. However, similar trends in terms of rotational docking are not seen, and the side inlets do not pose a clear advantage over the top inlet in terms of rotational docking ability.

F. Quantitative comparison of assembly schemes

In order to evaluate which scheme led to the most number of successful assemblies, a histogram showing the mean values of the two docking parameters for all initial tile conditions (both position and orientation) was plotted for the different assembly schemes studied (Fig. 14). The error bars in the histogram plot indicate the standard deviation in the docking parameter values for these schemes. This figure shows that schemes A2, B2, C2, and D2 have lower values of both $D_{x,y}$ as well as the standard deviation of $D_{x,y}$ as compared to schemes A1, B1, C1, and D1, respectively. This indicates, as previously discussed, that assembly schemes with multiple side inlets (schemes A2, B2, C2, and D2) led

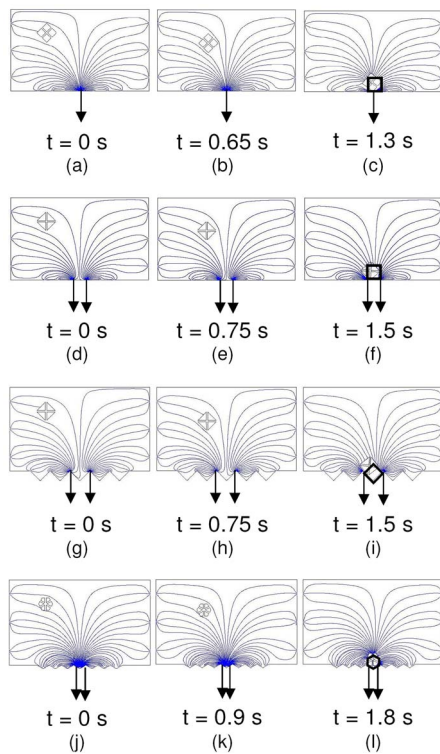


FIG. 13. (Color online) Time elapsed images showing tile locations for tiles with initial tile orientation $\psi=45^\circ/30^\circ$ and initial position $\varphi=30^\circ$: [(a)–(c)] scheme A2; [(d)–(f)] scheme B2; [(g)–(i)] scheme C2; [(j)–(l)] scheme D2. The black outlined squares and hexagons indicate the target tile locations, while the arrows indicate fluid outlets.

to more successful translational docking, both in terms of number of successful docking events as well as degree of success, compared to assembly schemes where there was a single top inlet directly above the outlet. Also, on comparing the different assemblies, we found that scheme D2 had the lowest mean value of $D_{x,y}$, making it the most successful scheme of the various schemes considered in terms of the translational docking parameter. Schemes A2 and B2 were

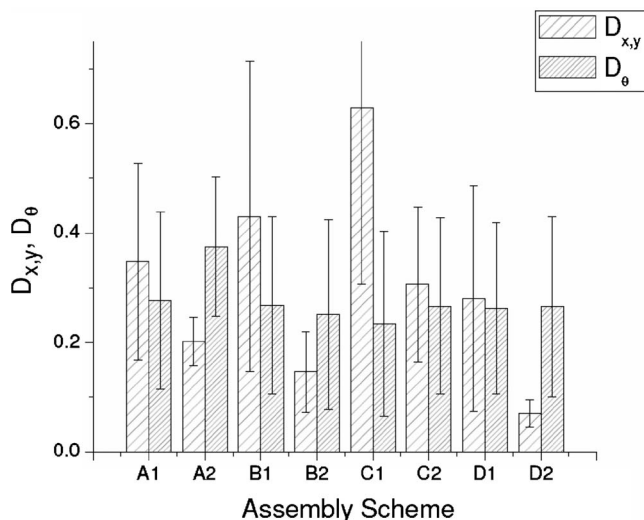


FIG. 14. Histogram comparing different assembly schemes based on docking parameters.

also found to work well, with a low mean value of the $D_{x,y}$ docking parameter and low standard deviation. Thus, the use of inlet jets orthogonal to the direction of desired tile motion worked well in directing the tile to the target location.

There was, however, a large amount of scatter in the D_θ values for all the assembly schemes considered, indicated by the large values of standard deviation in the D_θ histogram, and there was no clear indication of which scheme had the best rotational docking capabilities. However, a good trend did emerge when the assembly schemes were judged based on both the translational and rotational docking parameters. It is clear from Fig. 14 that schemes B2 and D2 were among the most successful assembly schemes, combining good translational docking and rotational docking properties. As mentioned previously though, the hexagonal tile in scheme D2 did not undergo significant rotation due to the flow field, while scheme B2 showed a definite tendency to rotate the square tile to a 0° angle. Thus scheme D2 can be used to successfully assemble a hexagonal tile provided an alternate scheme exists to initially orient the hexagonal tile. Similarly, scheme B2 can be used as a successful assembly scheme for square tiles.

V. CONCLUSIONS

The work we have presented here describes a 2D fluid mechanics model that predicts the motion of a tile through a fluidic chamber due to translational forces and rotational torques on the tile while capturing relevant 3D effects, as was seen by comparison with 3D simulations and experimental results. This 2D approach serves to significantly reduce computational time and resources and as such is more amenable for extension to a multitile environment. The model was also used to quantitatively compare different assembly schemes using two docking parameters. Since the initial tile position and orientation in an assembly chamber are stochastic, we attempted to arrive at an assembly procedure that led to successful assembly over the broadest range of initial tile conditions. On comparing different assembly schemes, it was found that the use of side ports in a chamber, with inlet jets orthogonal to the direction of tile motion, gave the most successful tile assembly results. Additionally, it was found that these jets were successful in correcting the initial orientation of a square tile, and the use of a dual outlet configuration served to align the square tile on a flat substrate. It was also found that the flow field did not significantly affect the initial orientation of a hexagonal tile which docked at angles similar to the initial angle of the tile.

ACKNOWLEDGMENTS

This work was supported by the National Science Foundation under Grant No. CMMI-0634652, “Hierarchical Microfabrication: Actively Programmable Multi-level Fluidic Self-Assembly.”

¹M. J. Madou, *Fundamentals of Microfabrication: The Science of Miniaturization* (CRC, Boca Raton, 2002).

²G. M. Whitesides and B. Grzybowski, “Self-assembly at all scales,” *Science* **295**, 2418 (2002).

- ³D. Philp and J. F. Stoddart, "Self-assembly in natural and unnatural systems," *Angew. Chem.* **35**, 1155 (1996).
- ⁴R. J. Jackman, S. T. Brittain, A. Adams, M. G. Prentiss, and G. M. Whitesides, "Design and fabrication of topologically complex, three-dimensional microstructures," *Science* **280**, 2089 (1998).
- ⁵M. B. Cohn, K. F. Böhringer, J. M. Noworolski, A. Singh, C. G. Keller, K. Y. Goldberg, and R. T. Howe, "Microassembly technologies for MEMS," in *Proceedings of the SPIE Conference on Micromachining and Microfabrication Process Technology IV*, Santa Clara, CA (SPIE, Bellingham, 1998), pp. 2–16.
- ⁶K. F. Böhringer, R. S. Fearing, and K. Y. Goldberg, *The Handbook of Industrial Robotics* (Wiley, New York, 1999), Chap. 55.
- ⁷G. M. Whitesides and M. Boncheva, "Beyond molecules: Self-assembly of mesoscopic and macroscopic components," *Proc. Natl. Acad. Sci. U.S.A.* **99**, 4769 (2002).
- ⁸E. Winfree, F. R. Liu, L. A. Wenzler, and N. C. Seeman, "Design and self-assembly of two-dimensional DNA crystals," *Nature (London)* **394**, 539 (1998).
- ⁹B. Olenyuk, J. A. Whiteford, A. Fechtenkötter, and P. J. Stang, "Self-assembly of nanoscale cuboctahedra by coordination chemistry," *Nature (London)* **398**, 796 (1999).
- ¹⁰N. Bowden, A. Terfort, J. Carbeck, and G. M. Whitesides, "Self-assembly of mesoscale objects into ordered two-dimensional arrays," *Science* **276**, 233 (1997).
- ¹¹U. Srinivasan, D. Liepmann, and R. T. Howe, "Microstructure to substrate self-assembly using capillary forces," *J. Microelectromech. Syst.* **10**, 17 (2001).
- ¹²U. Srinivasan, M. A. Helmbrecht, C. Rembe, R. S. Muller, and R. T. Howe, "Fluidic self-assembly of micromirrors onto microactuators using capillary forces," *IEEE J. Sel. Top. Quantum Electron.* **8**, 4 (2002).
- ¹³X. Xiong, Y. Hanein, J. Fang, Y. Wang, W. Wang, D. T. Schwartz, and K. F. Böhringer, "Controlled multibatch self-assembly of microdevices," *J. Microelectromech. Syst.* **12**, 117 (2003).
- ¹⁴J. Chung, W. Zheng, T. J. Hatch, and H. O. Jacobs, "Programmable reconfigurable self-assembly: Parallel heterogeneous integration of chip-scale components on planar and nonplanar surfaces," *J. Microelectromech. Syst.* **15**, 457 (2006).
- ¹⁵H. J. Yeh and J. S. Smith, "Fluidic self-assembly for the integration of GaAs light-emitting diodes on Si substrates," *IEEE Photonics Technol. Lett.* **6**, 706 (1994).
- ¹⁶W. Zheng and H. O. Jacobs, "Shape-and-solder-directed self-assembly to package semiconductor device segments," *Appl. Phys. Lett.* **85**, 3635 (2004).
- ¹⁷Y. H. Ye, S. Badilescu, V. V. Truong, P. Rochon, and A. Natansohn, "Self-assembly of colloidal spheres on patterned substrates," *Appl. Phys. Lett.* **79**, 872 (2001).
- ¹⁸M. Golosovsky, Y. Saado, and D. Davidov, "Self-assembly of floating magnetic particles into ordered structures: A promising route for the fabrication of tunable photonic band gap materials," *Appl. Phys. Lett.* **75**, 4168 (1999).
- ¹⁹M. Tanase, D. M. Silevitch, A. Hultgren, L. A. Bauer, P. C. Searson, G. J. Meyer, and D. H. Reich, "Magnetic trapping and self-assembly of multi-component nanowires," *J. Appl. Phys.* **91**, 8549 (2002).
- ²⁰Y. Higuchi, T. Kusakabe, T. Tanemura, K. Sugano, T. Tsuchiya, and O. Tabata, "Manipulation system for nano/micro components integration via transportation and self-assembly," in *Proceedings of the 21st IEEE International Conference Micro Electro Mechanical Systems (MEMS)*, Tucson, AZ (IEEE, New York, 2008), Catalog No. CFP08MEM-PRT, pp. 836–839.
- ²¹M. Krishnan, M. T. Tolley, H. Lipson, and D. Erickson, "Directed hierarchical self assembly—Active fluid mechanics at the micro and nanoscales," in *Proceedings of the ASME International Mechanical Engineering Congress and Exposition (IMECE)*, Seattle, WA (ASME, New York, 2007), p. 41784.
- ²²M. T. Tolley, A. Baisch, M. Krishnan, D. Erickson, and H. Lipson, "Interfacing methods for fluidically-assembled microcomponents," in *Proceedings of the 21st IEEE International Conference on Micro Electro Mechanical Systems (MEMS)*, Tucson, AZ (IEEE, New York, 2008), Catalog No. CFP08MEM-PRT, pp. 1073–1076.
- ²³R. Ganguly, A. P. Gaiand, and I. K. Puri, "A strategy for the assembly of three-dimensional mesoscopic structures using a ferrofluid," *Phys. Fluids* **17**, 057103 (2005).
- ²⁴R. Ganguly, B. Zellmer, and I. K. Puri, "Field-induced self-assembled ferrofluid aggregation in pulsatile flow," *Phys. Fluids* **17**, 097104 (2005).
- ²⁵D. Liu, M. R. Maxey, and G. E. Karniadakis, "Simulations of dynamic self-assembly of paramagnetic microspheres in confined microgeometries," *J. Micromech. Microeng.* **15**, 2298 (2005).
- ²⁶C. H. Lee, Y. Lu, and A. Q. Shen, "Evaporation induced self assembly and rheology change during sol-gel coating," *Phys. Fluids* **18**, 052105 (2006).
- ²⁷K. F. Böhringer, U. Srinivasan, and R. T. Howe, "Modeling of capillary forces and binding sites for fluidic self-assembly," in *Proceedings of the 14th IEEE International Conference on Micro Electro Mechanical Systems (MEMS)*, Interlaken, Switzerland (IEEE, New York, 2001), Catalog No. 01CH37090, pp. 369–374.
- ²⁸S. Abbasi, A. X. Zhou, R. Baskaran, and K. F. Böhringer, "Part tilting in capillary-based self-assembly: Modeling and correction methods," in *Proceedings of the 21st IEEE International Conference on Micro Electro Mechanical Systems (MEMS)*, Tucson, AZ (IEEE, New York, 2008), Catalog No. CFP08MEM-PRT, pp. 1060–1063.
- ²⁹H. Onoe, K. Matsumoto, and I. Shimoyama, "Three-dimensional micro-self-assembly using hydrophobic interaction controlled by self-assembled monolayers," *J. Microelectromech. Syst.* **13**, 603 (2004).
- ³⁰C. K. Aidun, Y. N. Lu, and E. J. Ding, "Direct analysis of particulate suspensions with inertia using the discrete Boltzmann equation," *J. Fluid Mech.* **373**, 287 (1998).
- ³¹P. Cherukat and J. B. McLaughlin, "The inertial lift on a rigid sphere in a linear shear-flow field near a flat wall," *J. Fluid Mech.* **263**, 1 (1994).
- ³²J. Feng, H. H. Hu, and D. D. Joseph, "Direct simulation of initial value problems for the motion of solid bodies in a Newtonian fluid. Part 2: Couette and Poiseuille flows," *J. Fluid Mech.* **277**, 271 (1994).
- ³³J. Feng, H. H. Hu, and D. D. Joseph, "Direct simulation of initial value problems for the motion of solid bodies in a Newtonian fluid. Part 1: sedimentation," *J. Fluid Mech.* **261**, 95 (1994).
- ³⁴I. Kim, S. Elghobashi, and W. A. Sirignano, "On the equation for spherical-particle motion: effect of Reynolds and acceleration numbers," *J. Fluid Mech.* **367**, 221 (1998).
- ³⁵M. R. Maxey and J. J. Riley, "Equation of motion for a small rigid sphere in a nonuniform flow," *Phys. Fluids* **26**, 883 (1983).
- ³⁶H. M. Blackburn and R. D. Henderson, "A study of two-dimensional flow past an oscillating cylinder," *J. Fluid Mech.* **385**, 255 (1999).
- ³⁷S. M. Kang, H. C. Choi, and S. Lee, "Laminar flow past a rotating circular cylinder," *Phys. Fluids* **11**, 3312 (1999).
- ³⁸J. D. Sherwood and H. A. Stone, "Added mass of a disc accelerating within a pipe," *Phys. Fluids* **9**, 3141 (1997).
- ³⁹R. L. Panton, *Incompressible Flow* (Wiley, Hoboken, 2005), Chap. 22.
- ⁴⁰G. K. Batchelor, *An Introduction to Fluid Dynamics* (Cambridge University Press, Cambridge, 2000), Chap. 4.